Magn Reson Med Sci 2019; 18; 88–95
doi:10.2463/mrms.tn.2017-0170
Published Online: May 16, 2018

TECHNICAL NOTE

3D Cones Acquisition of Human Extremity Imaging Using a 1.5T Superconducting Magnet and an Unshielded Gradient Coil Set

Ayana Setoi and Katsumi Kose*

We developed ultrashort echo-time (UTE) imaging sequences with 3D Cones trajectories for a home-built compact MRI system using a 1.5T superconducting magnet and an unshielded gradient coil set. We achieved less than 7 min imaging time and obtained clear *in vivo* images of a human forearm with a TE of 0.4 ms. We concluded that UTE imaging using 3D Cones acquisition was successfully implemented in our 1.5T MRI system.

Keywords: *gradient coil, magnetic resonance imaging, three-dimensional Cones, ultrashort echo-time*

Introduction

Ultrashort echo-time (UTE) MRI is widely used as a method of visualizing tissues with short T_2 or T_2^* such as cortical bones, tendons, and lung tissues.[1] Among several methods for UTE imaging, the most representative one is 3D radial imaging.[2] The advantages of 3D radial imaging are that this method is relatively easy to implement and is less susceptible to eddy current effects because there is no need to change the gradient field strength during the data acquisition period. However, there are several problems in practical 3D imaging because 3D radial acquisition has no flexibility in trajectory design and it is difficult to shorten the imaging time.

In contrast, UTE imaging using cones trajectory (3D Cones acquisition) can shorten the imaging time compared to 3D radial imaging. 3D Cones acquisition using a spiral-like trajectory on the surface of cones was proposed in 1995.[3] It has several advantages over 3D radial imaging, such as a flexible sequence design, highly efficient data collection, and robustness to motion and flow.[4] Therefore, there are several reports that 3D Cones acquisition has been used for sodium imaging,[5] coronary magnetic resonance angiography,[6] and musculoskeletal imaging.[7] However, there are several problems, such as difficulty in designing and controlling the gradient waveforms, and sensitivity to eddy fields and magnetic field inhomogeneity. For these reasons, there is a very limited number of reports on the implementation of 3D Cones acquisition. Therefore, it is challenging and interesting to implement 3D Cones acquisition in customized MRI systems.

In this study, we implemented 3D Cones sequences on a home-built MRI system for human extremities using a horizontal bore 1.5T superconducting magnet, and demonstrated the usefulness of 3D Cones acquisition for UTE imaging using imaging of a phantom, a biological sample, and a human forearm.

Materials and Methods

MRI system using a 1.5T superconducting magnet

An overview of the MRI system used in this study is shown in Fig. 1a. The system consisted of a horizontal bore superconducting magnet, a second-order shim coil set, an unshielded gradient coil set, a radio frequency (RF) coil, and a digital MRI transceiver (DTRX6; MRTechnology, Ibaraki, Japan).[8] The superconducting magnet (JMBT-1.5/280/SS; JASTEC, Kobe, Japan) had a 1.5T static magnetic field strength, a room temperature bore of 280-mm-diameter and 521-mm-length, and about 50-ppm magnetic field inhomogeneity over the 160-mm-diameter spherical volume. The room temperature shim coil set was designed after Roméo and Hoult and consisted of five second-order shim coils made of a 0.6-mm-diameter polyurethane (PU)-coated copper wire wound over an acrylic pipe (dimensions: outer diameter [o.d.]: 260 mm, inner diameter [i.d.]: 252 mm). The unshielded gradient coil set was designed using the target-field approach. The G_x and G_y coils were made of 0.4-mm-thick dual-layer etched printed boards with 175-μm-thick Cu foils (350 μm total thickness). These coils were cylindrically bent and attached on an acrylic pipe (dimensions: o.d.: 160 mm, i.d.: 152 mm, length: 370 mm). The G_z coil was wound over the G_x and G_y coils with a 1.4-mm-diameter PU-coated copper wire. The current efficiencies and DC resistance of the gradient coils G_x, G_y, and G_z

Institute of Applied Physics, University of Tsukuba, 1-1-1 Tennodai, Tsukuba, Ibaraki 305-8573, Japan
*Corresponding author, Phone: +81-298-53-5214, Fax: +81-298-53-5205, E-mail: kose@bk.tsukuba.ac.jp

Received December 1, 2017 | Accepted April 4, 2018

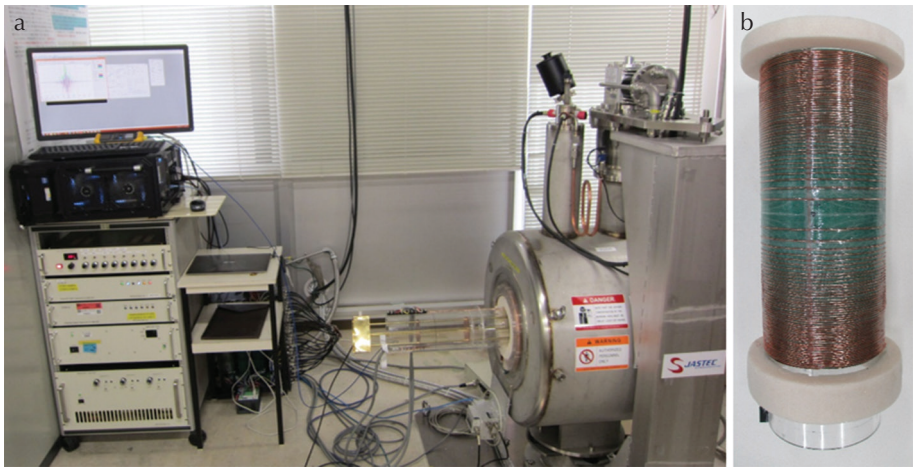

Fig. 1 (**a**) Overview of the MRI system using a 1.5T horizontal bore superconducting magnet (280 mm room temperature bore). (**b**) An unshielded gradient coil set wound over an acrylic pipe (260 mm outer diameter, 252 mm inner diameter).

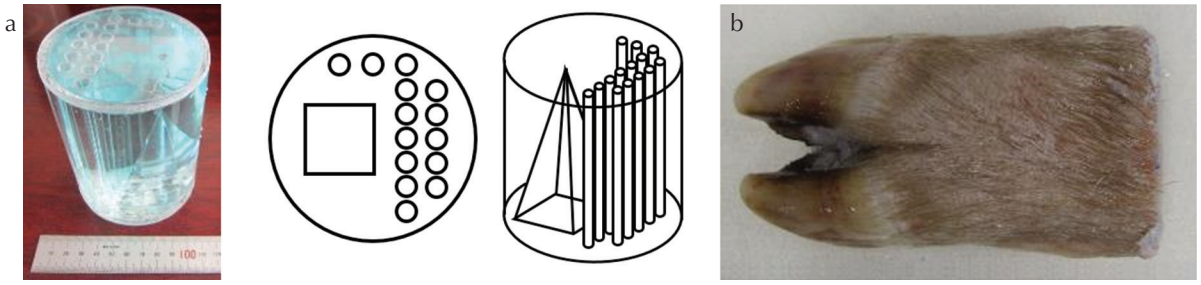

Fig. 2 (**a**) The overview, bottom view, and perspective view of the 3D water phantom made of acrylic round bars and an acrylic square pyramid attached in an acrylic cylindrical container filled with a $CuSO_4$ water solution ($T_1 = T_2 = 80$ ms). The inner diameter and the inner length of the water phantom were 82 and 100 mm, respectively. (**b**) Porcine hoof sample (maximum diameter = 72 mm, maximum length = 118 mm).

were 2.00, 1.93, and 2.51 mT/m/A and 1.16, 1.21, and 0.62 Ω, respectively. The maximum amplitudes and the slew rates of the gradient coils G_x, G_y, and G_z were 34, 32, and 50 mT/m and 80, 80, and 100 T/m/s, respectively. The RF coil was an eight-element linearly polarized birdcage coil (diameter 110, length 130 mm) with a resonance frequency of 63.93 MHz. The whole MRI system was controlled by the "Sampler 6" or "Digital Sequencer" software program (MRTechnology) running under the Windows 10 operating system (Microsoft, Seattle, WA, USA).

Samples

A water phantom used for the evaluation of image distortion and eddy current effects is shown in Fig. 2a. It comprised of 14 acrylic rods (diameter 8 mm) and an acrylic regular square pyramid ($40 \times 40 \times 80$ mm^3) fixed in an acrylic cylindrical container (dimensions: o.d.: 90 mm, i.d.: 82 mm, length: 108 mm) filled with a $CuSO_4$ water solution ($T_1 = T_2 = 80$ ms). A sample acquired from a porcine hoof is shown in Fig. 2b. A human forearm of a volunteer (male, 64-year-old) was used to demonstrate the feasibility of *in vivo* imaging after informed consent was obtained. The human volunteer measurement was performed based on the guideline of the ethical committee of the Faculty of Pure and Applied Sciences in University of Tsukuba.

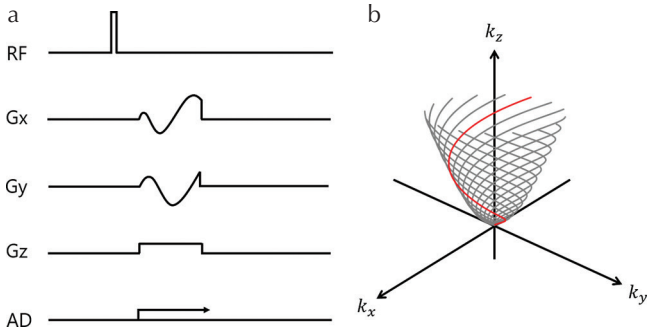

Fig. 3 (**a**) The pulse sequence diagram for the 3D Cones acquisition with 64 shots for each cone. The period and the interval of the data sampling were 1.44 ms and 5 µs. (**b**) One of the trajectories for the 3D Cones acquisition.

Pulse sequence design and image reconstruction

A typical pulse sequence diagram and the trajectory used in this study are shown in Fig. 3. The oscillating gradient waveforms (G_x and G_y) were designed using the waveforms of spiral imaging proposed by Glover[9] and Kodama et al.[10] The radial acquisition along the z-direction was made by a constant G_z gradient. The k-space trajectories for the 3D Cones acquisition were generated by a combination of the spiral trajectory in the k_x k_y plane and the radial trajectory along the k_z direction (Fig. 3b). The cone angle for the 3D

Cones trajectory was changed from 0 to π radian to cover an entire spherical volume in the *k*-space.

In the 3D Cones acquisition, the image matrix and the FOV were 128 × 128 × 128 and 128 × 128 × 128 mm^3, respectively. The number of shots per cone was 64. The period and interval of the data sampling were 1.44 ms and 5 ms, respectively. The number of cones was 128 for the water phantom and porcine hoof sample, and 64 and 128 for the human forearm. The TR of the 3D Cones acquisition was 200 ms for the water phantom and the porcine hoof sample and 100 ms for the human forearm. The TE of the 3D Cones acquisition was defined as the time between the start time of the application of the RF pulse and the start time of the readout gradients. TE was 0.4 ms for the water phantom and the human forearm, and 0.4 and 1.0 ms for the porcine hoof sample. The pulse width and flip angle of the RF pulse were 240 μs and 90°, respectively.

Because the pulse sequences of the 3D Cones acquisition had a very complicated structure, the sequences were implemented by the following two methods.

In the first method, the 3D Cones sequence was implemented as a collection of 2D spiral-like sequence files corresponding to one cone angle. This method was simple, and making sequence files was easy. However, the actual imaging time was longer than the nominal imaging time because of overhead time needed to input the sequence files into the data acquisition program. The nominal and actual imaging times for the water phantom and the porcine hoof sample were 13 min 39 s and 27 min 10 s, respectively.

In the second method, the 3D Cones sequence was implemented as one sequence file with a specialized sequence format. Although a customized sequence generation program was required, there was no overhead time during the data acquisition. We used this file format for *in vivo* imaging and the actual (= nominal) imaging time was 6 min 49 s and 13 min 39 s for 64 and 128 cone acquisitions (TR was 100 ms), respectively.

For comparison, we used conventional 3D gradient-echo (GRE) sequences. In the GRE sequence, TR was 200 ms for the water phantom and the porcine hoof sample and 100 ms for the human forearm. TE was 4.6 ms for the water phantom and 2.3 and 4.6 ms for the porcine hoof sample. The image matrix was 128 × 128 × 256 and 256 × 128 × 64 for the water phantom and the human forearm.

The image reconstruction for the 3D Cones acquisition (64 shots, 128 cones, and 288 sampling points for each trajectory) was performed using 3D fast Fourier transform after regridding the acquired signal data to the Cartesian coordinate 128 × 128 × 128 cubic grid points of the *k*-space. We used the nearest neighbor approximation for the regridding.

Linear eddy field measurements

We used a spherical phantom made of a plastic spherical container (outer diameter 25.4 mm) filled with a $CuSO_4$ water solution to measure linear eddy fields caused by gradient switching. We placed the phantom at the center of the gradient coil, and measured the linear eddy fields using the pulse sequence shown in Fig. 4, is as follows. First, a gradient pulse of 100 ms duration time was applied. A square RF pulse (pulse width: 40 μs) was applied after a delay time t_R from the falling edge of the gradient pulse. The temporal position of the gradient-echo peak was shifted by δt because the actual magnetic field gradient waveform was deformed by the induced linear eddy fields (Fig. 4). We repeated the pulse sequence while varying the delay time t_R (t_R = 0.01, 0.02, …, 100 ms) and the amplitude of the gradient pulse denoted by s (s = –32, –31, … +31), and measured the time shift δt.

The relation between the linear eddy field $e(t)$ and the time shift δt can be expressed as follows:

$$\int_{\Delta}^{\infty} s \cdot e(t)\,\mathrm{d}t = -G_r \delta t(t_R, s).$$

The integral of the linear eddy field $\int e(t)\,\mathrm{d}t$ can be obtained by finding the slope of the straight line of the $s - \delta t(t_R)$ graph plotted for each t_R. We performed curve-fitting to find the time constants and amplitudes using the equations, as follows.

$$\int e(t)\,\mathrm{d}t = -\sum_i a_i \tau_i \exp(-t/\tau_i),$$

where $\tau_i's$ are the decaying time constants and $a_i's$ are the amplitudes of the linear eddy field components.[11]

Linear eddy field estimation

The gradient waveforms of G_x and G_y vary sinusoidally with increasing amplitudes for the 3D Cones acquisition. Therefore, the eddy fields are always induced because the applied magnetic field gradient always changes. We estimated the linear eddy fields for the 3D Cones acquisition using the step response of the linear eddy fields measured in Fig. 4. The estimation was performed using convolution of the original (undeformed) gradient field waveform changing every 40 ms and the step response function measured by the experiments described above.

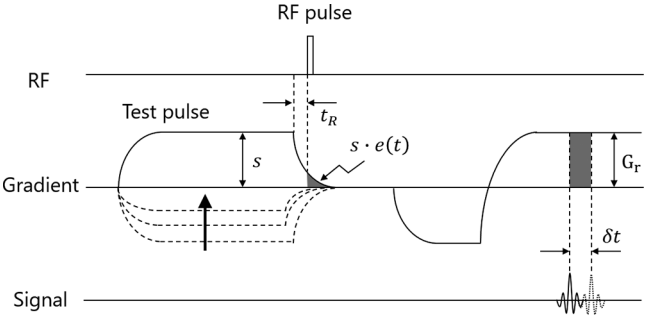

Fig. 4 Pulse sequence used to measure linear eddy fields. The duration of the gradient pulse was 100 ms and its amplitude was changed by 64 steps. A spherical water phantom (23.4 mm inner diameter) was used to observe the gradient echo signal. The typical echo time for the gradient echo signal was 20 ms. RF, radio-frequency.

Table 1 Time constants and relative amplitudes of the linear eddy fields

	G_x		G_y		G_z		
	Comp. 1	Comp. 2	Comp. 1	Comp. 2	Comp. 1	Comp. 2	Comp. 3
Time constant (ms)	0.0766	23.4	0.0455	23.5	0.128	10.4	249
Amplitude (%)	6.41	0.565	19.0	0.600	7.88	0.401	0.0352

Comp., component.

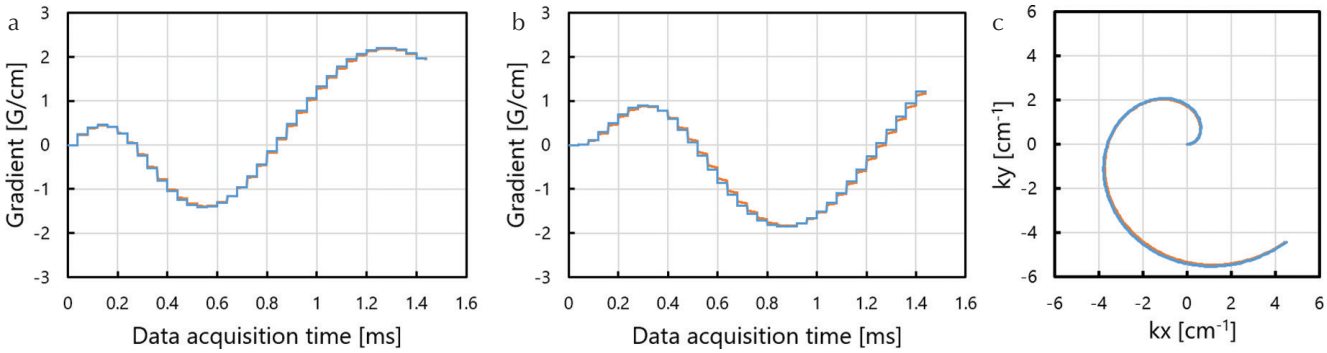

Fig. 5 The original (orange) and estimated (blue) waveforms of the magnetic field gradients, (**a**) Gx, (**b**) Gy. (**c**) *k*-space trajectories shown in the k_xk_y plane calculated using the gradient waveforms with and without the linear eddy fields. The orange and blue lines are trajectories with and without linear eddy fields.

Results

Linear eddy fields measured by the spherical phantom

The time constants and relative amplitudes for the linear eddy fields are listed in Table 1. The components for G_x and G_y are classified into two types of components, with short time constants (46–77 μs) with relative amplitudes of 6.4–19%, and with longer time constants (23.5 ms) with relative amplitudes of 0.57–0.6%. The components for G_z were classified into three types: The component with the shortest time constant (0.13 ms) with relative amplitude of 7.9%, that with the second shortest time constant (10 ms) with a relative amplitude of 0.4%, and that with the longest time constant (250 ms) with a relative amplitude of 0.035%.

The original waveforms of the magnetic field gradients G_x and G_y generated by the gradient coils and modified waveforms affected by the induced linear eddy fields are shown in Fig. 5a and b. Because the amplitude of the component with the shorter time constant for G_y was larger than that for G_x, the modified waveform of G_y was much more deformed than G_x. Because the relationship between the *k*-space trajectories and the gradient waveforms is expressed as

$$k(t) = \frac{\gamma}{2\pi}\int_0^t G(u)\,\mathrm{d}u,$$

the *k*-space trajectories with and without the effect of the linear eddy fields were calculated (Fig. 5c) using the gradient waveforms shown in Fig. 5a and b. The *k*-space trajectory with the effect of the linear eddy fields decreased in size by about 1.1% and became shorter by about 20 μs than that without the eddy field effect.

Images from the 3D Cones acquisition

Figure 6 displays the two-dimensional (2D) cross-sectional images selected from the 3D image datasets of the water phantom acquired with the (a) 3D Cones and (b) conventional 3D GRE sequences displayed at 10-mm intervals. We confirmed that the 3D Cones acquisition was correctly implemented because the 3D structure was clearly described. In the images from the 3D Cones acquisition, there was sample rotation in the axial plane depending on the *z*-coordinate. Next, we measured the rotation angle and plotted it against the *z*-coordinate (Fig. 7). While there was little change for the 3D GRE, a considerable parabolic change was clearly observed for the 3D Cones acquisition. Figure 8 shows line profiles of the central cross-sections of the 3D Cones and 3D GRE images measured along the array of the seven acrylic round bars. These images demonstrated only a slight decrease of the spatial resolution for the 3D Cones acquisition as shown by the arrows in the profiles.

The coronal image of the porcine hoof sample acquired with the conventional 3D GRE (TE was 4.6 ms) is shown in Fig. 9a. The axial images around the central positions of the six bones (the yellow lines in Fig. 9a) are shown in Fig. 9b-e. These were acquired with (b) 3D Cones (TE = 0.4 ms), (c) 3D Cones (TE = 1.0 ms), (d) 3D GRE (TE = 2.3 ms), and (e) 3D GRE (TE = 4.6 ms) sequences. The signal from the tissues with a short T_2^* such as the deep digital flexor tendon, was lost in Fig. 9e, but recovered in the images acquired with the 3D Cones acquisition (shown by the arrows).

Figure 10 shows the axial images selected from 3D image datasets of the human forearm acquired with the (a) 3D Cones (64 cones), (b) 3D Cones (128 cones), and (c) 3D

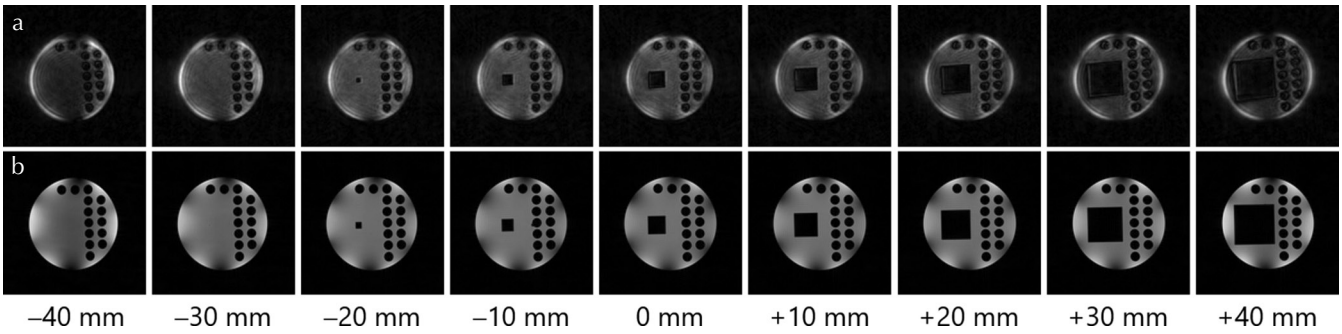

Fig. 6 Two-dimensional cross-sectional images selected from the 3D image dataset of the 3D water phantom acquired with the (**a**) 3D Cones, (**b**) conventional 3D GRE sequences, displayed at 10-mm intervals. Slight shrink and rotation of the 3D Cones images relative to the gradient-echo (GRE) images in the cross-sectional planes were observed.

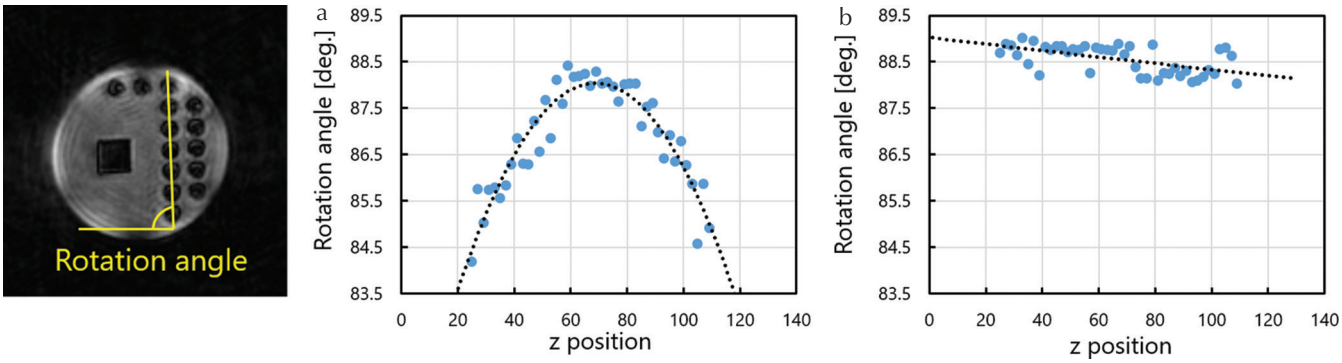

Fig. 7 Rotation angle measured in the axial plane plotted against the *z*-direction for the image acquired with the (**a**) 3D Cones and (**b**) 3D gradient-echo (GRE) sequences. The parabolic change of the rotation angle for the 3D Cones acquisition is remarkable.

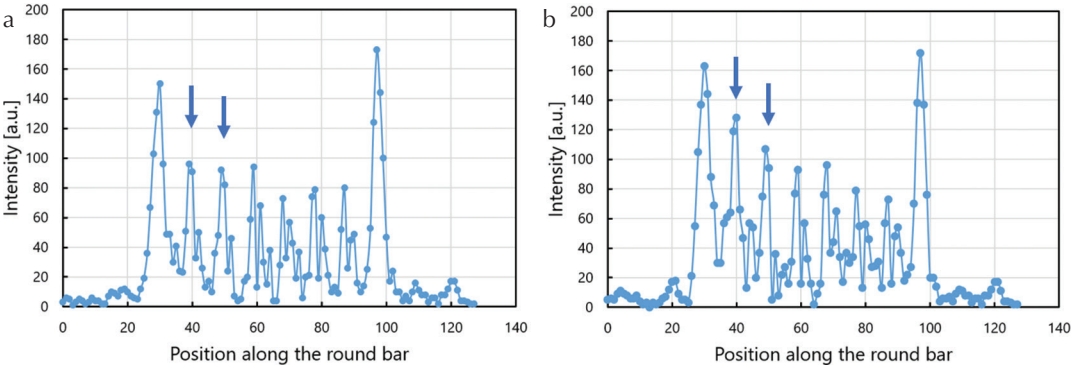

Fig. 8 Line profiles of the central cross-sections acquired with (**a**) 3D Cones and (**b**) 3D GRE images measured along the array of the seven acrylic round bars. The arrows shown in the profiles demonstrate a slight decrease of the spatial resolution for the image acquired with the 3D Cones sequence.

GRE sequences. For Fig. 10b, although the sampling density was higher than that in Fig. 10a by a factor of two, few changes were observed.

Discussion

Image distortion observed in the 3D Cones acquisition

For the conventional 3D GRE, about 1° of the image rotation in the 3D phantom from the left end to the right end was observed (Fig. 7). We think that this image rotation was mainly caused by a manufacturing error of the 3D water phantom.

In contrast, for the 3D Cones acquisition, a parabolic change of the image rotation angle was clearly observed along the z-direction. We believe that the parabolic change was caused by the eddy fields of higher-order terms proportional to z^2x and z^2y, because the linear eddy fields caused delay times of the gradient waveforms (Fig. 4), which in turn resulted in image rotation in the *xy* plane as is well known in spiral imaging.[10] As the data acquisition time was 1.44 ms in this study and the trajectory rotates about 1 turn for the 64-shot sequence, the angular velocity of the rotation was $2\pi/(1.44\ \mathrm{ms})$ or $1.3°/(5\ \mu\mathrm{s})$. The maximum rotation angle for the 3D Cones acquisition was about 4° (Fig. 7), corresponding to a delay time of about 16 µs of the gradient waveform at the both ends compared with the central axial plane. This value is reasonable because this is comparable to the delay time calculated for the trajectory (Fig. 5).

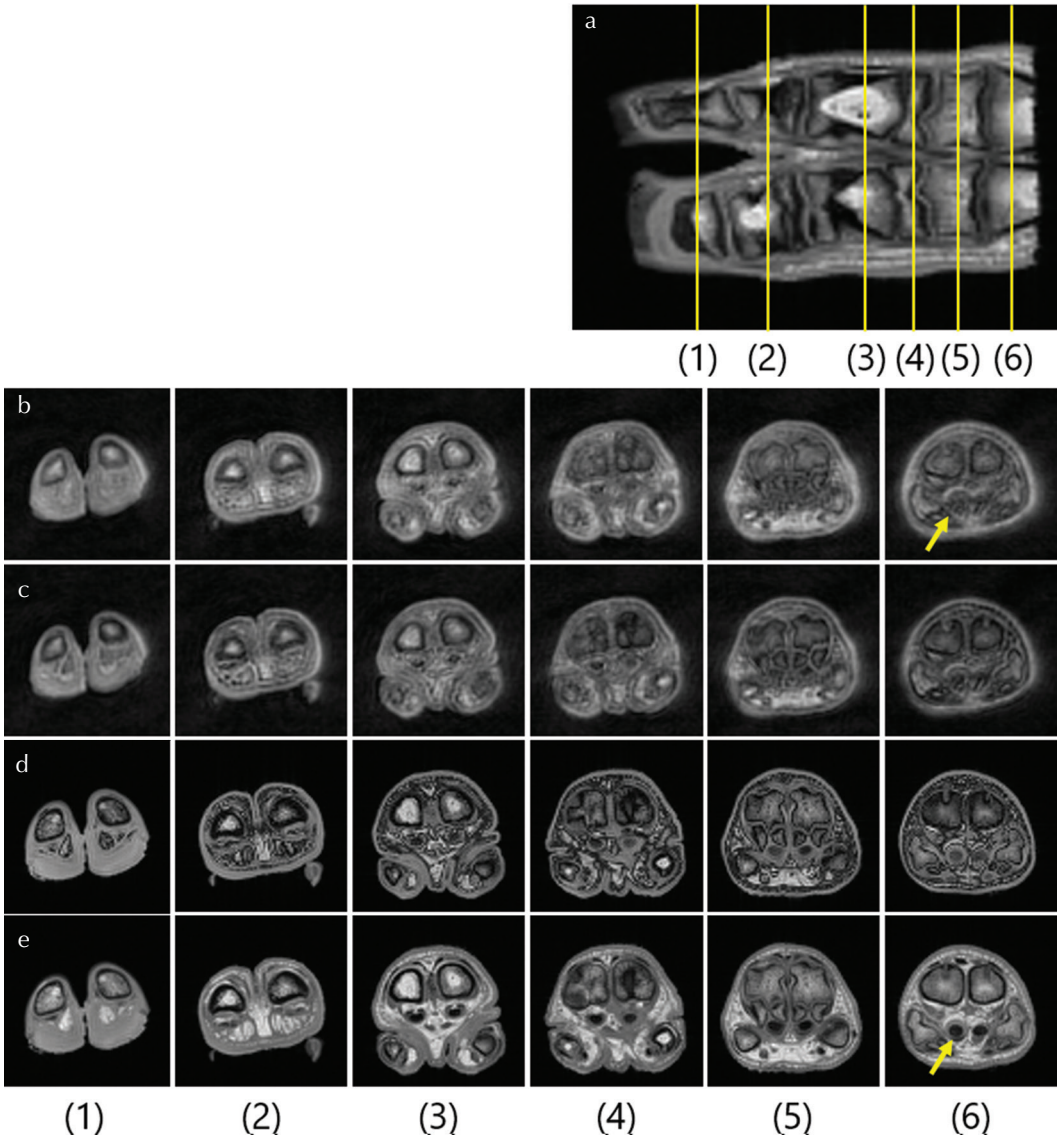

Fig. 9 (**a**) Coronal cross-sectional image selected from 3D image datasets of the porcine hoof sample acquired with the 3D gradient-echo (GRE) sequence (TR = 200 ms, TE = 4.6 ms). (**b**–**e**) Axial cross-sections acquired with (**b**) 3D Cones (TE = 0.4 ms), (**c**) 3D Cones (TE = 1.0 ms), (**d**) 3D GRE (TE = 2.3 ms), and (**e**) 3D GRE (TE = 4.6 ms) sequences. The positions for the cross-sections shown by the numbers (1–6) in the coronal image correspond to the axial cross-sections shown in (**b**–**e**). The signal from the tissues with a short T_2^* such as the deep digital flexor tendon was lost in Fig. 8(e) but recovered in Fig. 8(b) (the arrows).

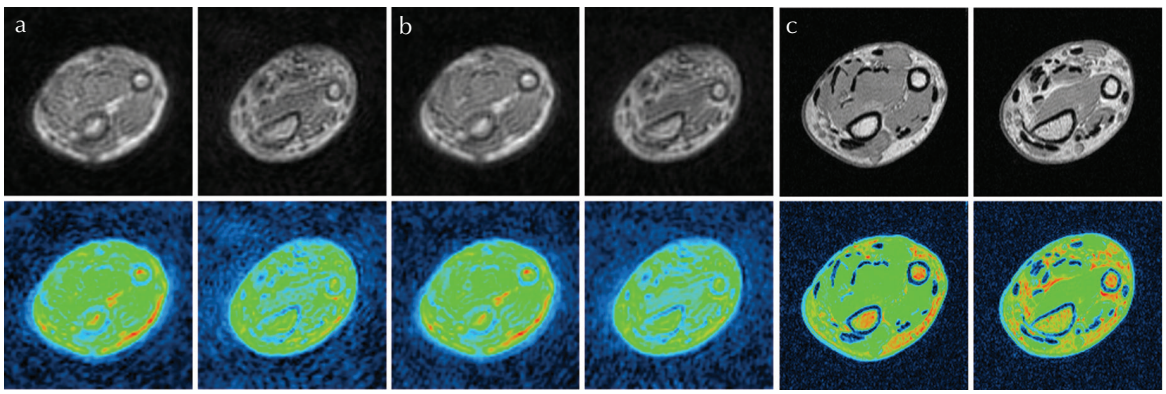

Fig. 10 Cross-sectional images selected from 3D image datasets of a human forearm acquired with (**a**) 3D Cones (64 cones), (**b**) 3D Cones (128 cones), (**c**) conventional 3D gradient-echo (GRE) sequences. Upper and lower images were displayed in gray and color scale for the identical images.

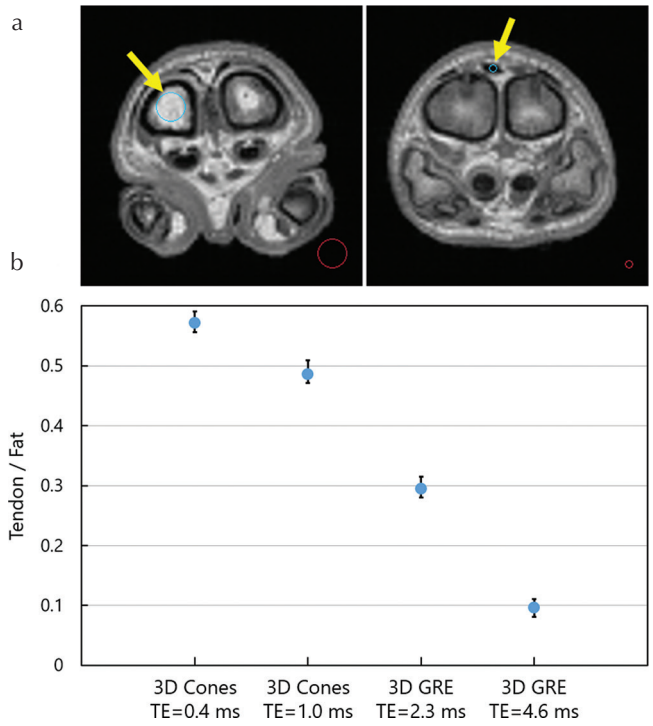

Fig. 11 (**a**) The digital extensor tendon (in the right image) and the bone marrow (in the left image) used for evaluation of the T_2^* contrast for the 3D Cones and 3D GRE images. (**b**) Relative image intensity of the distal extensor tendon normalized by the bone marrow image intensity.

Image contrast for the biological sample

As shown in Figs. 9 and 10, tissues with short T_2^* that were not visualized in the 3D GRE images were visualized in the images acquired with the UTE 3D Cones sequences. To demonstrate the T_2^* contrast in the biological samples more clearly, we calculated the relative intensity of the digital extensor tendon normalized by that of the bone marrow of the trabecular bone in the proximal phalanx as shown in Fig. 11a. Because the bone marrow of peripheral bones is almost pure fatty tissue and the T_2^* of the bone marrow proton is determined by the susceptibility difference between the trabecular bone and the bone marrow, the T_2^* of the bone marrow protons that depends on the trabecular bone density is known to be more than about 10 ms.[12] Therefore, the MR image intensity for the tendon with T_2^* of around 1 ms can be evaluated by the ratio of the image intensity of the tendon to that of the bone marrow. The ratio is plotted in Fig. 11b, which clearly demonstrates the correct T_2^* contrast for these sequences.

Total imaging time for in vivo *imaging*

In this study, we achieved an imaging time of less than seven minutes for the human forearm by reducing TR and the number of cones. Although this imaging time is sufficient for clinical applications, some discussion is required for the reduction in TR and the number of cones.

First, because the T_1 of most human tissues except fat tissues is around 1000 ms, a TR of 100 ms gives heavily T_1 weighted images or low signal-to-noise ratio (SNR) images because of T_1 saturation effect. To overcome this problem, the use of a small flip-angle excitation and rewinding of the readout gradient may be effective. However, because the rewinding of the readout gradient in 3D Cones acquisition is a very difficult technique, the use of small flip-angle excitation optimized for TR would be a practical choice.

Second, the number of cones should be carefully determined because it affects spatial resolution and image artifacts caused by the regridding error. To reduce the regridding error, a larger number of cones is preferable. However, because of the trade-off between the number of the cones and imaging time, we must find the best combination for *in vivo* imaging.

Overcome of hardware imperfection

High-performance MRI hardware is indispensable with UTE imaging using 3D Cones acquisition. In this subsection, we will focus on the following two topics.

First, intense magnetic field gradients are required. For 3D Cones acquisition, the longer the data acquisition time is, the more image blur is caused by the effect of the static magnetic field inhomogeneity and the T_2^* effect. Therefore, the data acquisition time needs to be shortened as much as possible to suppress image blur or distortion. Therefore, we believe that an intense magnetic field gradient system is essential in UTE imaging using 3D Cones acquisition.

Second, the constructed system needs to be free from eddy current effects. As shown in Table 1, there were two kinds of the linear eddy fields with different origins in our system. We think that the eddy field component with the shorter time constant was caused by the high-frequency electromagnetic shielding of the RF coil (copper foil, 60 μm thick, 150 mm diameter, and 200 mm long), that was caused by the radiation shield of the superconducting magnet (aluminum cylinder, 2 mm thick, 302 mm o.d., 482.5 mm long) with the longer time constant. To overcome the eddy field problem, we think use of a field camera system to measure eddy fields to correct the k-trajectory is promising.

Conclusion

We developed UTE imaging sequences with 3D Cones trajectories for a compact MRI system using a 1.5T horizontal bore superconducting magnet and an unshielded gradient coil set. Eddy current effects were quantitatively evaluated using eddy field measurements and 3D Cones imaging of a 3D water phantom. Short T_2^* tissues of a biological sample and an *in vivo* human forearm were visualized using short TE (0.4 ms) 3D Cones sequences. We concluded that UTE imaging for human extremities was successfully implemented with 3D Cones acquisition in our customized compact 1.5T MRI system.

Acknowledgment

This study was supported by the Japan Science and Technology Agency.

Conflicts of Interest

The authors declare that they have no conflicts of interest.

References

1. Chung EY, Du J, Chung CB. UTE imaging in the musculoskeletal system. J Magn Reson Imaging 2015; 41:870–883.
2. Rahmer J, Börnert P, Groen J, Bos C. Three-dimensional radial ultrashort echo-time imaging with T_2 adapted sampling. Magn Reson Med 2006; 55:1075–1082.
3. Irarrazabal P, Nishimura DG. Fast three dimensional magnetic resonance imaging, Magn Reson Med 1995; 33:656–662.
4. Gurney PT, Hargreaves BA, Nishimura DG. Design and analysis of a practical 3D cones trajectory. Magn Reson Med 2006; 55:575–582.
5. Boada FE, Shen GX, Chang SY, Thulborn KR. Spectrally weighted twisted projection imaging: reducing T_2 signal attenuation effects in fast three-dimensional sodium imaging. Magn Reson Med 1997; 38:1022–1028.
6. Addy NO, Ingle RR, Wu HH, Hu BS, Nishimura DG. High-resolution variable-density 3D cones coronary MRA. Magn Reson Med 2015; 74:614–621.
7. Carl M, Bydder GM, Du J. UTE imaging with simultaneous water and fat signal suppression using a time-efficient multispoke inversion recovery pulse sequence. Magn Reson Med 2016; 76:577–582.
8. Hashimoto S, Kose K, Haishi T. Development of a pulse programmer for magnetic resonance imaging using a personal computer and a high-speed digital input-output board. Rev Sci Instrum 2012; 83:053702.
9. Glover GH. Simple analytic spiral k-space algorithm. Magn Reson Med 1999; 42:412–415.
10. Kodama N, Setoi A, Kose K. Spiral MRI on a 9.4 T vertical-bore superconducting magnet using unshielded and self-shielded gradient coils. Magn Reson Med Sci 2018; 17:174–183.
11. Bernstein MA, King KF, Zhou XJ. Eddy-current compensation, In: Handbook of MRI pulse sequences: Burlington, MA, Elsevier Academic Press: 2004; 316–331.
12. Ford JC, Wehrli FW. In vivo quantitative characterization of trabecular bone by NMR. Magn Reson Med 1991; 17:543–551.